

Article

Dynamic Charge Acceptance Compared to Electrochemical Impedance Spectroscopy Parameters: Dependencies on Additives, State of Charge, and Prior Usage

Sophia Bauknecht ^{1,*}, Julia Kowal ^{1,*}, Jochen Settelein ², Markus Föhlisch ³ and Eckhard Karden ⁴¹ Electrical Energy Storage Technology, Technische Universität Berlin, 10587 Berlin, Germany² Fraunhofer Institute for Silicate Research ISC, Neunerplatz 2, 97082 Würzburg, Germany³ MOLL Batterien GmbH, Angerstraße 50, 96231 Bad Staffelstein, Germany⁴ Ford Research & Innovation Center Aachen, 52072 Aachen, Germany

* Correspondence: sophia.bauknecht@tu-berlin.de (S.B.); julia.kowal@tu-berlin.de (J.K.)

Abstract: The goal of this work was to predict the dynamic charge acceptance (DCA) for cells using different additives on the negative electrode from the evaluation of small-signal measurements by electrochemical impedance spectroscopy (EIS). Thereby, various operating points were evaluated, such as state of charge (SoC) and prior usage (charge or discharge). The 2V test cells under investigation utilized plates of enhanced flooded 3P2N battery cells (EFB). They contained three positive and two negative electrodes. The latter varied in their additive composition. In total, eight different negative electrodes were investigated, five including specially synthesized amorphous carbon as an additive, two with unknown additive mixes, and one including a commercially available carbon black. The best parameters for predicting the DCA were found within the first semicircle of the negative half-cell spectra measured during a superimposed charging current.

Keywords: dynamic charge acceptance; electrochemical impedance spectroscopy; equivalent circuit model; lead-acid batteries



Citation: Bauknecht, S.; Kowal, J.; Settelein, J.; Föhlisch, M.; Karden, E. Dynamic Charge Acceptance Compared to Electrochemical Impedance Spectroscopy Parameters: Dependencies on Additives, State of Charge, and Prior Usage. *Batteries* **2023**, *9*, 263. <https://doi.org/10.3390/batteries9050263>

Academic Editor: Sylvain Franger

Received: 8 February 2023

Revised: 17 March 2023

Accepted: 21 April 2023

Published: 8 May 2023



Copyright: © 2023 by the authors. Licensee MDPI, Basel, Switzerland. This article is an open access article distributed under the terms and conditions of the Creative Commons Attribution (CC BY) license (<https://creativecommons.org/licenses/by/4.0/>).

1. Introduction

Driven by the need to reduce emissions, battery performance became increasingly important in automotive applications. Furthermore, the function of automotive batteries shifted from starting, lighting, and ignition to providing significant contributions to a vehicle's performance. Stop/start and regenerative braking are the hybridization features for micro-hybrid vehicles. Thereby, the engine is stopped automatically when the vehicle stops, thus reducing emissions. To maximize its effectiveness, as much energy as possible must be recovered and stored within the battery during vehicle deceleration. The main factor limiting the ability to capture this energy is the battery's dynamic charge acceptance (DCA) at partial state of charge (SoC). Numerous testing methodologies have been developed to characterize the DCA of automotive batteries: single-pulse tests [1], the stand-alone DCA EN test [2], and more complex cycling tests [3,4].

The DCA of lead-acid batteries (LABs) in operation is not very consistent and hard to predict since it is influenced by many factors. Some of the main factors influencing on DCA are:

- SoC (a lower SoC results in higher DCA [5–7]);
- Short- and long-term history (Higher DCA can be found after prior discharge compared to prior charge [5,8–10]. Lower DCA can be found after prior discharge at a low current rate compared to discharge at a high current rate [5]. DCA degradation can be found after extended rest time [5,8]);
- Electrolyte concentration and stratification (higher DCA results from lower electrolyte concentration [11,12] as well as lower stratification [11,13,14]);

- Temperature (higher temperatures result in higher DCA [5,6,13]); and
- Additives used within the electrodes [5,9,10,15–20].

A previous publication has shown that it is possible to predict DCA by using electrochemical impedance spectroscopy (EIS) [21]. Thereby, DCA was determined according to EN 50342-6:2015 [2]. The results were correlated with the parameters gained from the negative half-cell EIS measured with a superimposed charging current at 80% SoC [21]. A good correlation was found between the DCA and the resistance values of the first semicircle [21]. However, the EIS was only tested at one SoC after being previously discharged.

In addition to the already shown qualitative predictability of the DCA of test cells with different carbon additives using EIS [21], the scope of this work is to predict DCA at different working points. Thereby, it had to be evaluated whether the influence of the SoC and the short-term history on DCA can also be seen in EIS.

2. Experimental

2.1. Test Cell Preparation

A total of eight different negative active mass (NAM) formulations were studied. Among them, five amorphous carbon powders, which only varied in their external surface, provided by the Fraunhofer ISC and synthesized by the Bavarian Center for Applied Energy Research [22], were used. The synthesis of these five carbons [23] and their physical properties [9] are described in the literature. The specific surface area and the specific pore volume of the five different amorphous carbon powders were very similar [9]. The significant variation of the specific external surface area (S_{ext}) and, thereby, the variation of the average particle size (d_{part}) is given in Table 1. From previous studies it is known that the external surface area is directly proportional to DCA according to an EN test [24]. Next to the five synthesized amorphous carbons, two commercially used additive mixes which enhance DCA (referred to as C_X and C_Y) and a commercially available carbon black, used as reference (Ref), were included in this study.

Table 1. Textural properties of five synthesized carbon materials and a commercial reference CB (adapted ref. [9]).

Material ID	S_{ext} of Carbon	d_{part}
EFB + C_1	$7.1 \text{ m}^2 \text{ g}^{-1}$	633 nm
EFB + C_2	$20.3 \text{ m}^2 \text{ g}^{-1}$	221 nm
EFB + C_3	$50.4 \text{ m}^2 \text{ g}^{-1}$	88 nm
EFB + C_4	$92.1 \text{ m}^2 \text{ g}^{-1}$	48 nm
EFB + C_5	$159.3 \text{ m}^2 \text{ g}^{-1}$	27 nm
EFB + C_X	-	-
EFB + C_Y	-	-
EFB + Ref	$28 \text{ m}^2 \text{ g}^{-1}$	104 nm

Paste mixing was done on a laboratory scale with an identical mixing routine for all additives under inspection. The basic paste recipe was not changed, but the amount of water was varied to control mass penetration and paste viscosity. The amount of water needed was not directly linked to carbon's external surface area. One paste mixture included:

- Lead oxide (1500 g);
- Water (194 ± 16 g, depending on water absorption of carbon);
- Diluted sulfuric acid ($\text{SD } 1.4 \text{ g} \cdot \text{cm}^{-3}$, 120 g);
- Barium sulfate (12 g);
- Vanisperse (3 g);
- Carbon additive (1.0 wt% = 15 g, for C_X and C_Y unknown).

After paste mixing, the active material was pasted manually on industrially manufactured starter battery grids (143 mm \times 113 mm) where $106 \text{ g} \pm 1 \text{ g}$ of active material was used per plate. For the EFB + C_X and the EFB + C_Y test cells, concasted grids were

used. For all other paste mixes, gravity casted grids were used. The electrodes were cured under moderate temperatures and a defined atmosphere. In the first step, high humidity of >95% RH at 40 °C was kept for 18 h to form tribasic lead sulfate. During the second curing step, the electrodes were dried, and residual lead content was reduced at increasing temperatures from 50 °C to 60 °C over a period of 24 h. The humidity was decreased during the second step from >95% RH to approximately 10% RH due to opening of the vent of the curing box. The completed plates were weighed, and only plates of 154 ± 7 g were used for cell preparation.

The negative plates were used to build 3P2N 2 V, 20 Ah EFB with eight different NAM additives. The nominal capacity of 20 Ah was chosen to guarantee typical NAM utilization levels, whereas the actual capacity of the test cells was much larger due to an excess of acid volume and PAM content. Consequently, SOC was scaled to nominal capacity within this work. To maximize the influence of the additives in the NAM, the negative plates were bound to be the limiting factor within the cells. All test cells used the same industrial manufactured positive plates. Furthermore, the same current collector and the same cell case were used for testing. All tests were conducted in a climate chamber, minimizing outer influences.

In the following, all currents were normalized to I_{20} , which is the current used for a 20 h complete discharge to determine the capacity (C_{20}) defined by the EN standard. A gentle formation procedure was used, with constant current charging of $3 \cdot I_{20} = 3$ A at room temperature of 25 °C up to $6 \cdot C_n = 120$ Ah (40 h), where C_n is the nominal capacity of the test cell. After formation, the acid density of all cells was adjusted to 1.29 g cm^{-3} at 100% SoC and all cells were filled up to an equal level. After the acid adjustment, all test cells were finalized by charging with a constant current of $0.5 \cdot I_{20} = 0.5$ A for 10 h to avoid acid stratification caused by the acid adjustment.

2.2. Constant Current Discharge

Before further testing, several constant-current C_{20} discharge cycles were conducted prior to the DCA (EN) test, shown in Table 2. These were used to ensure similar behaviors and capacities of all test cells. During the C_{20} test, the test cells were discharged with a constant current of $I_{20} = 1$ A until the cut-off voltage of 1.75 V was reached. In European EFB (and AGM) designs, the discharge capacity is typically acid-limited. However, within the test cell, there was an unavoidable acid overage, especially in the outside pores of the outer plates [25]. To avoid an unusually deep discharge of the active material, an additional cut-off condition of 22 h was supplemented.

Table 2. Test matrix.

Test Sequence	Batch 1	Batch 2	Batch 3
C_{20}	X	X	X
Single-pulse CA	X	X	
I_c at 80% SoC	X	X	X
I_d at 90% SoC	X	X	X
I_r at 80% SoC	X	X	X
I_d at 80% SoC		X	
LSM pictures	X	X	
EIS			X

2.3. Dynamic Charge Acceptance

Two different charge acceptance tests were executed. The first charge acceptance test based on the EN 50342-6:2015 where the DCA (I_{DCA}) results out of three parts: namely, after prior charge (I_c) at 80% SoC, after prior discharge (I_d) at 90% SoC, and during real start-stop micro-cycles (I_r) at 80% SoC [2]. At the named state of functions, the test cells were charged with 20 pulses, each 10 s long, with a voltage limit of 2.4 V. The average charging current during these pulses was the evaluation criterion for the DCA performance,

typically normalized to the capacity of the battery or test cell. Further explanation of the original DCA EN test usage at cell level is given in [10]. Within this work, only two parts out of the DCA EN test are shown, after charge (I_c) at 80% SoC and after prior discharge (I_d). However, I_d was conducted at 80% SoC rather than at 90% SoC. This way, both histories could be compared without any SoC influence.

The second test used was a charge acceptance single-pulse test for 10 s up to 2.4 V, based on the Japanese standard [1]. Similar to the DCA EN test the average charging current during this pulse was the evaluation criterion for this test as well, which was normalized to the capacity too. The standard only tests the charge acceptance after prior discharge at one specific SoC. To evaluate SoC influences and the effects of the short-term history, it was necessary to modify the test procedure to match the requirements. Therefore, the fully charged test cell was discharged with $1 \cdot I_{20} = 1$ A until the target (between 95% and 50%) SoC. Afterwards, the cells were rested for 16 h before the pulse test. This way, the charge acceptance after prior discharge was determined. To determine the charge acceptance after prior charge, the cells were discharged to 0% SoC and charged with $1 \cdot I_{20} = 1$ A, with a voltage limit of 2.6 V, until the target SoC afterwards. After the cells rested for 16 h, the pulse test was executed. A similar DCA test for SoC influence testing on VRLA batteries was already proposed by Smith et al. [6]. In contrast to their procedure, the test cells within this work were recharged not only before but also in between all charge acceptance tests. This way, it can be assured that the targeted SoC was actually investigated without any summed-up errors of previous charge acceptance tests. The charging regime used after each charge acceptance test, independent of the prior usage, was according to the EN standard [26]: $5 \cdot I_{20}$, for 24 h with a maximum voltage limit of 2.66 V and rest for at least 16 h before starting the following sequence. A schematic visualization of the preconditioning for the DCA single-pulse test is shown in Figure 1. The tests were executed at 25 °C within a climate chamber using 50 A channels of the Digatron power electronics MCT 50/100/200-06-13(12) ME. The test matrix visualizing the test order is shown in Table 2.

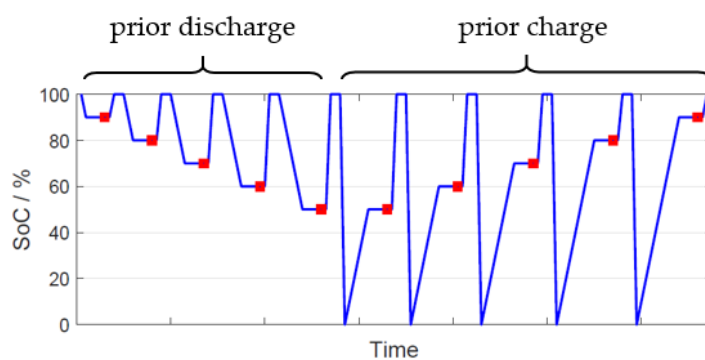


Figure 1. Schematic visualization of the preconditioning (prior discharge and charge, visualized in blue) for the charge acceptance single-pulse measurement (execution marked red).

2.4. Test Cell Preparation for Laser Scanning Microscopy

To investigate the morphological NAM differences corresponding to the starkly differing DCA after charge and after discharge, the test was stopped at 80% SoC after prior charge or discharge, and a 20 h rest time before the I_c or I_d measurement was started, respectively. Plate samples for laser scanning microscope (LSM) pictures were taken for EFB + C_X and EFB + C_Y test cells. These cell types were chosen since they showed significant differences between I_c and I_d .

For LSM measurements, the examined cell was opened, the cell stack was taken out, and a negative electrode was separated. Keeping the exposure to air as short as possible (under 1 min), the plates were cleaned in a beaker using isopropanol. Isopropanol was used as a non-reactive substance to clean off the electrolyte (sulfuric acid) from the negative plate. This way, further reactions, such as the growth of lead sulfate crystals, could be avoided. One washing consisted of five steps. Each step took 30 min with continuous

stirring. Thereby, the electrodes were rinsed off without using mechanical forces and possibly destroying the microscopic structure of the negative electrode. The isopropanol was replaced after each step, keeping the concentration gradient between the washing medium and the substance left in the pores high. Right after the washing procedure, the electrodes were dried in a vacuum oven at 60 °C for 24 h. The dried plates were scanned using LSM. LSM pictures were taken at three different heights (top, middle, and bottom) of the test cell. At each height, five different frames were taken and compared to ensure a uniform surface.

2.5. Electrochemical Impedance Spectroscopy

To receive valuable EIS measurement data, the battery should be kept in a stationary or at least in a quasi-stationary state during each measurement. Regardless, EIS measurements at various SoC (50% till 90% SoC in 5% steps adjusted based on Ah counting) with different superimposed currents ($I_{DC} = 0A, \pm 0.5 \cdot I_{20}, \pm 1 \cdot I_{20}, \pm 2 \cdot I_{20}$ and $\pm 4 \cdot I_{20}$) and with different histories (prior charging or prior discharging) were to be investigated. The testing profile is shown in Figure 2a. The test started with a freshly charged cell, which was discharged stepwise from 90% SoC down to 50% SoC, using a current of $1 \cdot I_{20}$. At each step, EIS was executed, marked with red rectangles in Figure 2a. First, an EIS measurement without any superimposed current ($I_{DC} = 0A$) was executed, followed by EIS with various superimposed charge and discharge currents. This measurement principle follows the micro-cycling approach introduced by Karden et al. [27] and has already been used in previous work [21]. During the micro-cycling approach, the cells were cycled by approximately $\pm 2.5\%$ SoC around the targeted SOC, visualized in Figure 2d. The cycles should not be larger to stay in the stationary state (regarding the SoC) during one EIS measurement. Figure 2c shows the superimposed current for investigating one SoC, and the resulting voltage is shown in Figure 2b. One impedance spectrum was recorded during each discharging and charging period, starting after 1% SoC change during each new superimposed current. This way, the rapid voltage change, where the cells were in a non-stationary state (in regard to the voltage), was not recorded during EIS. When the lowest step of 50% SoC was reached, the cells were fully recharged according to the EN standard [26]. This has two advantages: Firstly, during the whole discharge history containing micro-cycles at multiple SoCs, small errors of the superimposed DC currents and little asymmetrical AC currents during the EIS measurement all added up to the overall SoC error. To neglect this error, the cells were fully charged before starting the next phase. Secondly, during a full charge, all coarse sulphate crystals, accruing during the micro-cycles, were dissolved, and the cells started fresh into the second part, the charge history. After the complete charge, the cells were discharged to 0% SoC and recharged again to 50% SoC to start the charge phase. Now the cells were charged stepwise from 50% SoC up to 80% SoC using $1 \cdot I_{20}$. Again, at each step, the micro-cycle approach and EIS measurements were executed, marked with red in Figure 2a.

Pretests showed that it was not possible using the same micro-cycling approach, shown in Figure 2b–d, at each SoC step. At high SoC and for high superimposed currents, a voltage overshoot accrued during the micro-cycles. This voltage overshoot counteracted the basic requirement for using EIS: the system under inspection had to be stationary, linear, and causal. However, the system was not stationary anymore if the voltage showed an overshoot. Therefore, superimposed currents had to be limited at a high SoC to avoid voltage overshoots above 2.4 V, which could provoke a non-stationary state, with regards to the voltage of the cell. Therefore, at high SoC, only spectra with $I_{DC} = 0 A$ and $\pm 0.5 \cdot I_{20}$ were taken. For lower SoCs also, superimposed currents $\pm 1 \cdot I_{20}, \pm 2 \cdot I_{20},$ and $\pm 4 \cdot I_{20}$ were used. After prior charge, the voltage overshoots were more distinct compared to those after discharge. Therefore, EIS after prior charge was only possible up to 80% SoC. The micro-cycles of each superimposed current were repeated three times. Only the last impedance spectra with superimposed charge and discharge currents were investigated. Within this work, especially the negative half-cell spectra were evaluated to identify the influence of

NAM additives. Tests conducted before the EIS measurement procedure are summarized in Table 2. All EIS measurements were performed within a climate chamber at 25 °C to enable a stationary state with regards to the temperature. The most important measurement parameters are summarized in Table 3.

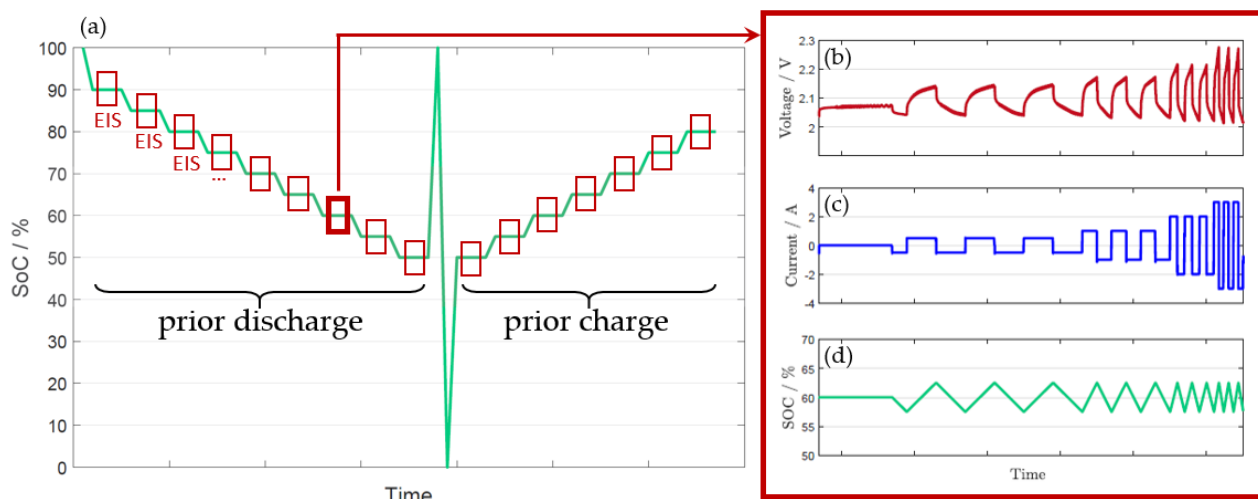


Figure 2. Schematic visualization of (a) the complete EIS measurement after prior discharge and charge and a zoom into the micro-cycle EIS procedure visualizing (b) voltage, (c) current, and (d) SoC at 60% SoC.

Table 3. EIS test parameters (adapted ref. [21]).

Parameter	Value
I_{DC}	0 A, $\pm 0.5 \cdot I_{20}$, $\pm 1 \cdot I_{20}$, $\pm 2 \cdot I_{20}$ and $\pm 4 \cdot I_{20}$
investigated SoC	50% till 90% SoC in 5% steps
investigated history	prior charge and discharge
$I_{AC,max}$	0.5 A
f_{min}	10 mHz
f_{max}	6.5 kHz
number of measurement points	8 frequencies per decade
T	25 °C
Δ SoC	$\pm 2.5\%$

The EIS measurements were recorded using a Digatron EISmeter 2-20-4. Half-cell spectra were measured using a hydrogen reference electrode Gaskatel 88010 from Gaskatel Gesellschaft für Gassysteme durch Katalyse und Elektrochemie mbH, Kassel, Deutschland.

The data processing, fitting, and parameter determination were already described in the authors' previous paper [21]. Summarizing, the obtained EIS data were preprocessed to avoid systematic errors, e.g., due to violations of the stationarity. First, a Kramers–Kronig (K–K) transformation was used to verify that the data were stable and causal and that the real and the imaginary parts were interdependent [28,29]. The measurement data points were compared with the K–K transformation. If the absolute error was larger than 1.5 m Ω or the ratio of the error to the absolute value of the impedance was greater than 3%, the data points were not evaluated any further. Figure 3 shows a complete EIS spectrum and indicates which data points were thrown out and which were used for further evaluation based on the K–K transformation. Afterwards, the distribution of relaxation times (DRTs) was used to analyze the number of processes and their characteristic frequencies. The number of processes identifies the number of resistance–capacity (RC) elements necessary for representing the spectra with an equivalent circuit model (ECM) and even allows their quantification [30,31]. Thereby, a valid ECM and starting parameters for fitting were chosen based on the DRTs.

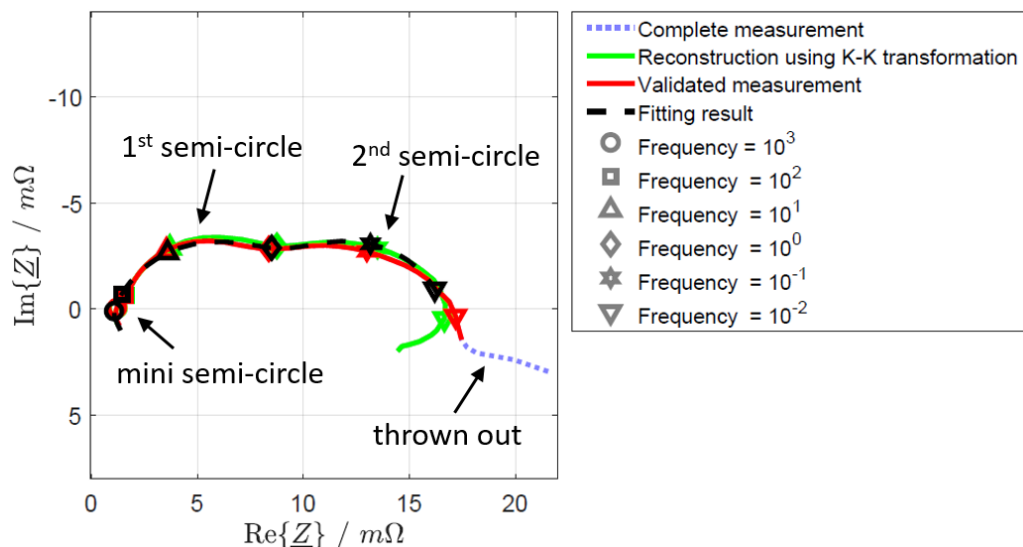


Figure 3. A sample EIS measurement, the evaluated part and the fit using the ECM.

The EIS measurements were evaluated using an equivalent circuit model (ECM). The ECM consists of internal resistance, an inductance, and three constant phase elements (CPE), shown in Figure 4.

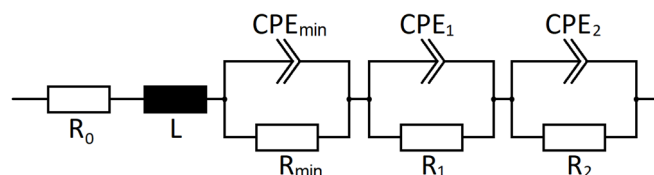


Figure 4. ECM for the EIS data of the negative half-cell (adjusted from [21]).

For the evaluation, the high-frequency part of the spectra remained very similarly independent of the investigated SoC, pre-histories, or the carbon additives used within the test cells. Therefore, the internal resistance, inductance, and one CPE describing the high-frequency part and the mini semicircle of the spectra were fitted but kept constantly independent of the investigated SoCs, pre-histories or the carbon additives used within the test cells. This way, some fitting parameters were excluded from influencing the remaining parameters, and the comparison between these remaining parameters and the DCA was clearer. Only the parameters of the first and second semicircle were variable and were described by resistance and capacitance. Both were connected by their time constant. However, the time constant did not obtain more information and was not visualized within this work. A spectrum is shown in Figure 4, marking the evaluated measurement data and comparing it to the fitting result using the described ECM.

3. Results and Discussion

3.1. Constant Current Discharge

The test results of the C_{20} constant discharging test are shown in Figure 5. Due to the acid surplus within the test cells, all test cells exceeded the expected 20 h discharge time, already discussed in previous work [25]. Nevertheless, the C_{20} test showed similar capacities and discharge curves for all test cells. Differences within later DCA or EIS tests were, therefore, assumed to originate from differences caused by the different additives.

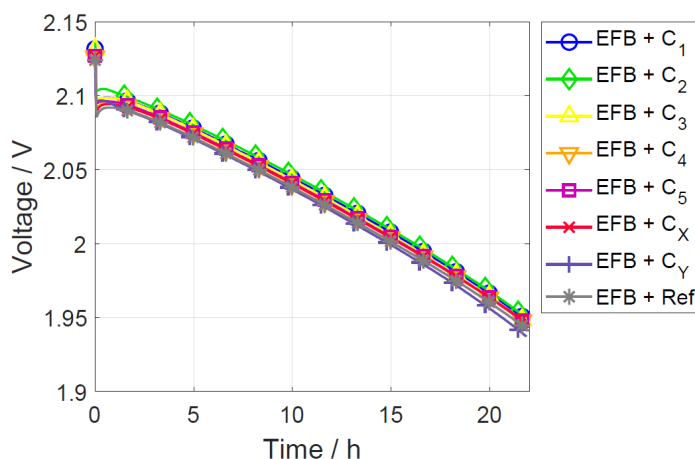


Figure 5. C₂₀ constant current discharge: voltage curves.

3.2. Influence of Prior Usage on DCA and EIS

In Figure 6a, I_c (DCA after prior charge) at 80% SoC is shown for all eight types of test cells. I_c at 80% SoC was tested using three similar test cells for each different additive type (except C₂, which could only be tested with one test cell). For each carbon additive, the average DCA result and the variation were visualized. To compare the influence of prior usage, I_d (DCA after prior discharge) at 80% SoC is shown in Figure 6b. I_d at 80% SoC was only conducted with one test cell for each carbon additive. I_c at 80% SoC was very small compared to I_d at 80% SoC.

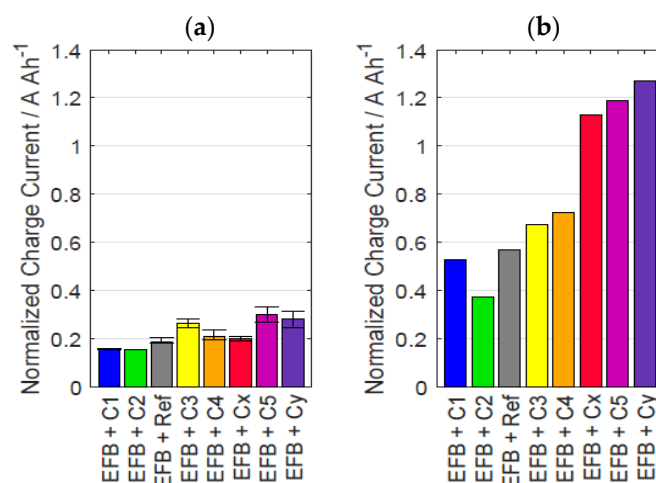


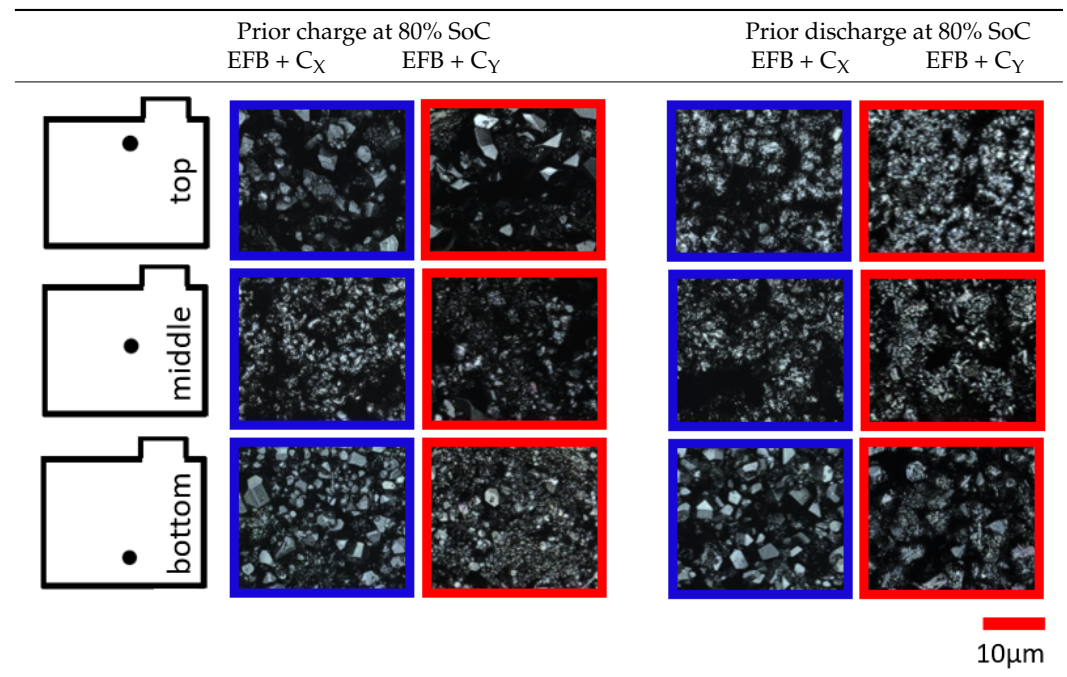
Figure 6. Partial DCA (EN) test results: (a) I_c at 80% SoC, (b) I_d at 80% SoC.

The test cells are ordered within Figure 6 according to their expected DCA result. The order of the DCA could not conclusively be identified for I_c at 80% SoC since all test cells had DCA values within the range of errors. However, I_d at 80% SoC increased in the following order: C₂ < C₁ < Ref < C₃ < C₄ < C_X < C₅ < C_Y. I_d at 80% SoC results of the five tailored carbons lined up (except C₁ and C₂, whose DCA test results are reversed) according to their external surface areas and was in agreement to the literature [24]. The higher the external surface area, the higher the DCA.

Differences in the geometric plate surface structure were investigated using LSM in order to investigate the correlation to differences in DCA, especially between I_c and I_d . Table 4 shows the LSM pictures after prior charge and after discharge for the two different EFB + C_X and EFB + C_Y test cells at three different electrode positions (top, middle, and bottom). These cell types were chosen since they showed significant differences between I_c and I_d . For the bottom part, the existence of superficial dense sulfate layers resulted

from stratification and stand times during initial cycling. This structure was independent of the additives used and remained unchanged after a charge and subsequent discharge. After prior charge, both cell types showed multiple coarse lead-sulfate crystals of several micrometers in size at the top of the cells. By contrast, after discharge, the PbSO_4 crystals were mostly dissolved, and only small crystals remained at the top of the negative plates. The coarse crystals after charge and fine crystals after discharge were expected to be identified. However, differences between $\text{EFB} + \text{C}_X$ and $\text{EFB} + \text{C}_Y$ should also be noticeable, at least after discharge, where the $\text{EFB} + \text{C}_X$ and $\text{EFB} + \text{C}_Y$ cells conducted different DCA as well. Significant differences between $\text{EFB} + \text{C}_X$ and $\text{EFB} + \text{C}_Y$ could be identified neither after prior charge nor after discharge within the LMS pictures. However, it is known that at 80% SoC, the active material consists of 60% pores [32]. For this reason, it is likely that most of the DCA-relevant processes were conducted within the pores, which would not be visible with an LSM. In the LSM pictures, only the plate surfaces could be shown, which should not be misinterpreted to show a situation representative of the overall active material since the surface inside the pores could be presented at all.

Table 4. LSM picture of the negative plate surface after charge and after discharge of the $\text{EFB} + \text{C}_X$ and the $\text{EFB} + \text{C}_Y$ test cell at the top, middle, and bottom.



To predict these DCA test results using EIS, it was necessary to investigate the same short-term and long-term history and the same SoC. There were EIS measurements and their fitting results after prior discharge at 90% SoC (Appendix A Figures A1 and A2), at 80% SoC (Appendix A Figures A3 and A4), and after prior charge at 80% SoC (Appendix A Figures A5 and A6). In the following, the I_c results, shown in Figure 6a, were compared with EIS taken after prior charge at 80% SoC. I_d results, shown in Figure 6b, were compared with EIS taken after prior discharge at 80% SoC. The correlations between the DCA and the EIS parameters $1/R_1$ (Figure 7), $1/R_2$ (Figure 8), CPE_1 (Figure 9), and CPE_2 (Figure 10) are shown.

The DCA test results for I_c were low and high for I_d , resulting in clustering of the data points in different sections within the figures, depending on the prior usage. Furthermore, the regression line was plotted for all values of I_c and I_d , and the correlation coefficients,

meaning a statistical relationship between two parameter sets, are given in Table 5. The correlation coefficient used was determined by:

$$R^2 = 1 - \frac{RSS}{TSS}$$

where R^2 is the correlation coefficient, RSS is the sum of squares of residuals, and TSS is the total sum of squares. The correlation coefficient is in the range from -1 to $+1$, where ± 1 indicates the strongest possible correlation.

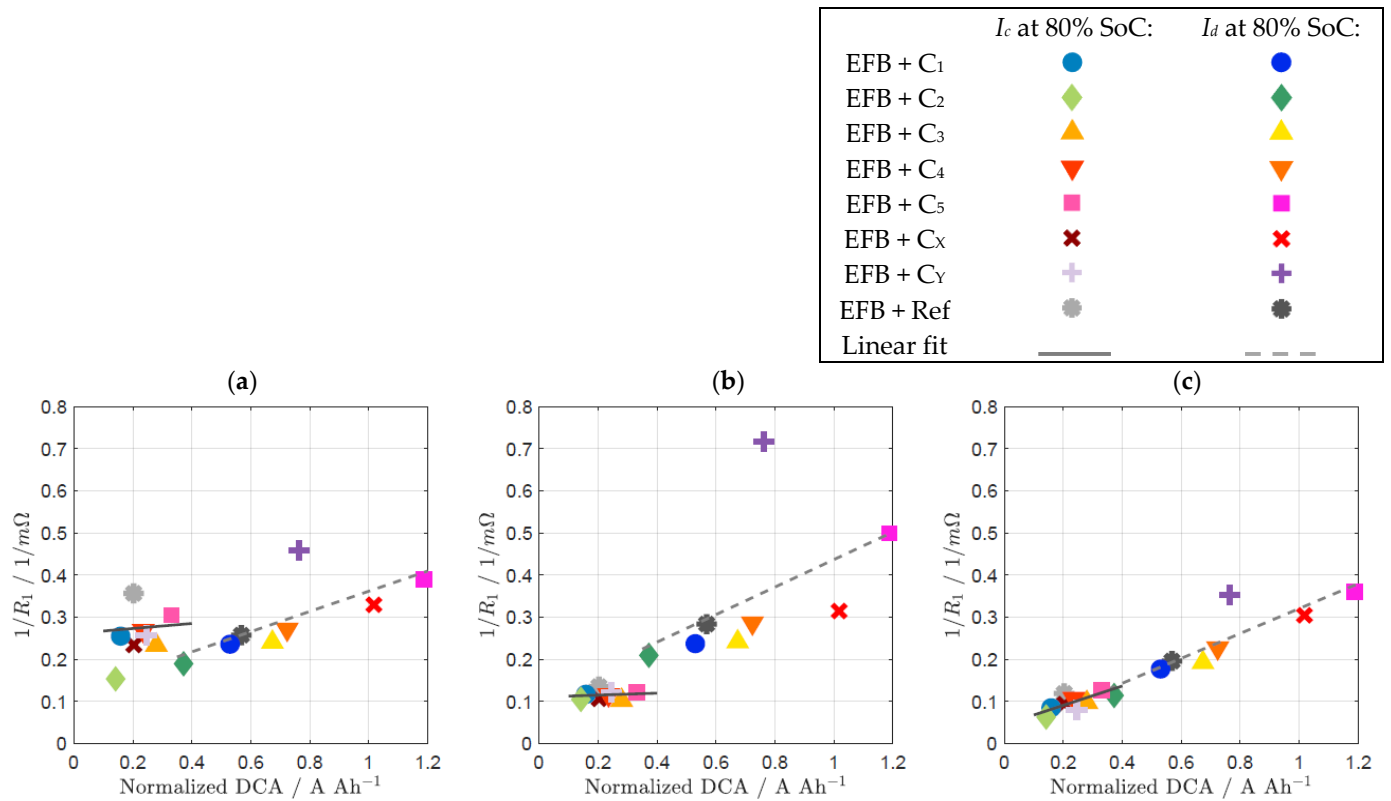


Figure 7. R_1 compared to DCA with $I_{DC} =$ (a) $-0.5 \cdot I_{20}$, (b) 0DC and (c) $+0.5 \cdot I_{20}$.

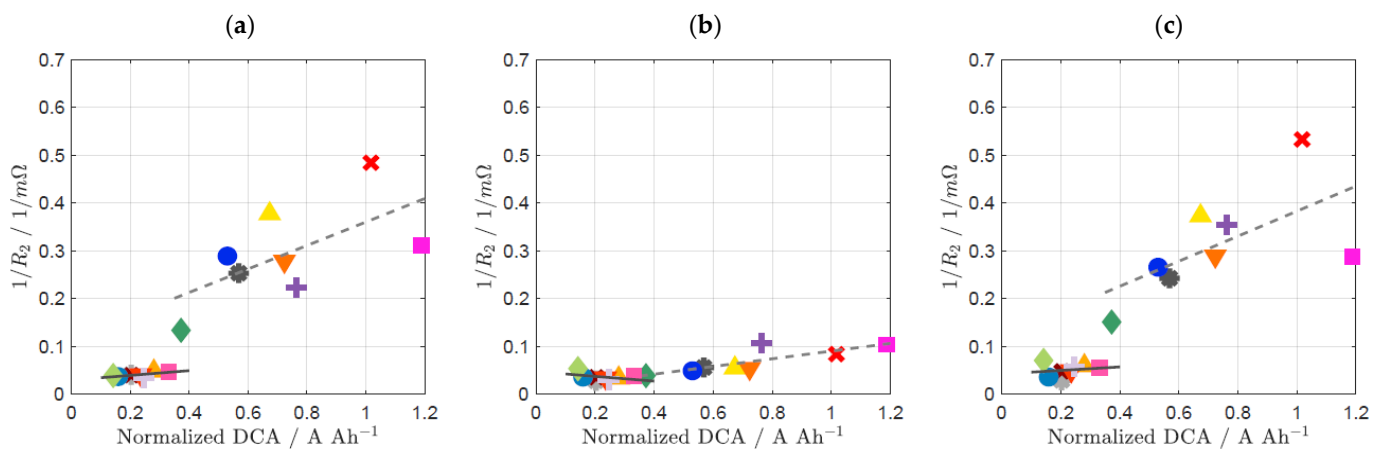


Figure 8. R_2 compared to DCA with $I_{DC} =$ (a) $-0.5 \cdot I_{20}$, (b) 0DC, and (c) $+0.5 \cdot I_{20}$.

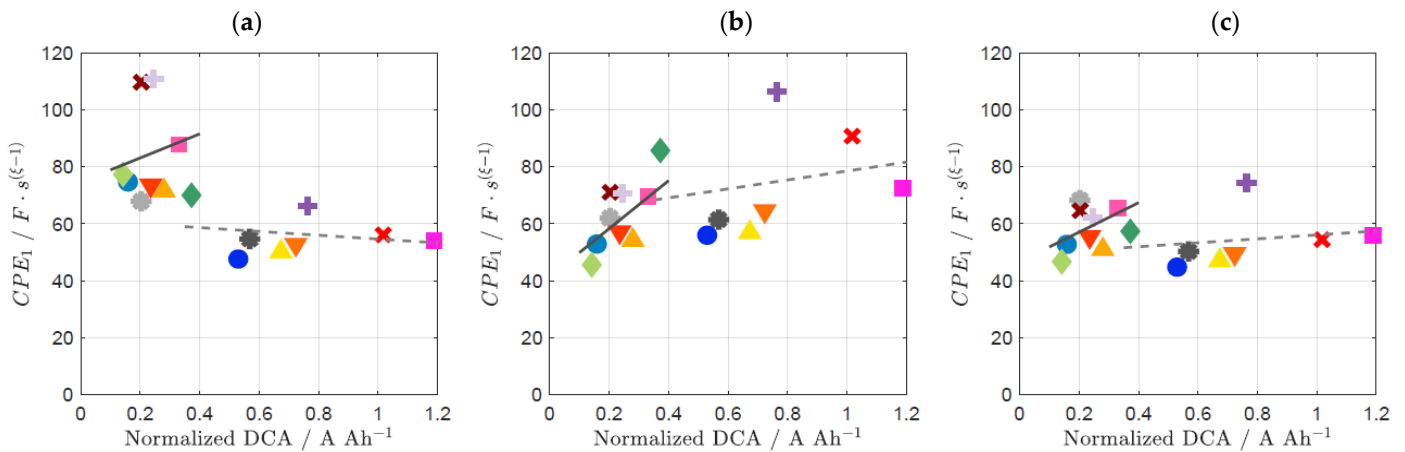


Figure 9. CPE_1 compared to DCA with $I_{DC} =$ (a) $-0.5 \cdot I_{20}$, (b) 0DC, and (c) $+0.5 \cdot I_{20}$.

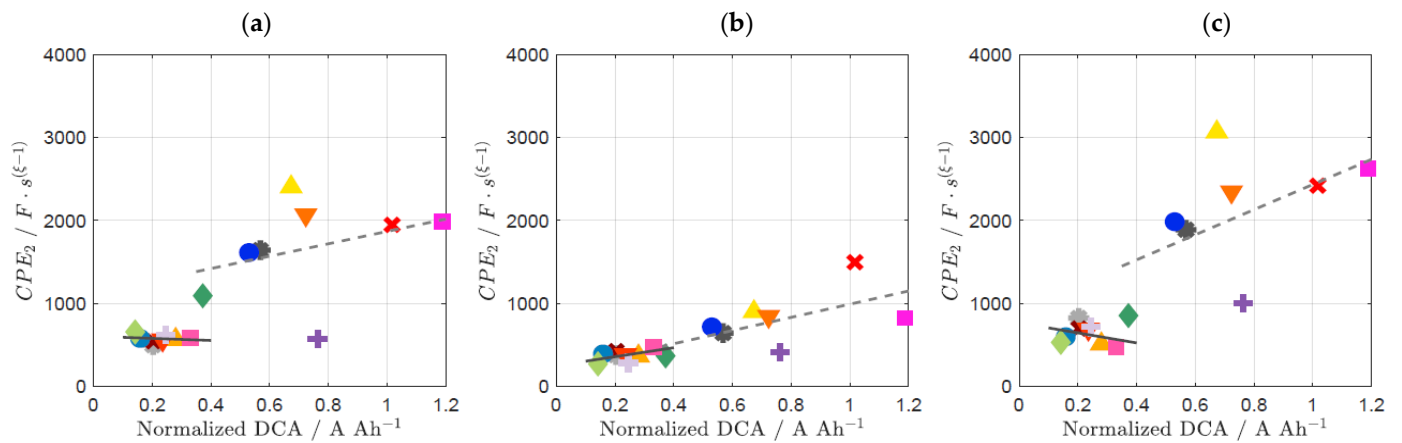


Figure 10. CPE_2 compared to DCA with $I_{DC} =$ (a) $-0.5 \cdot I_{20}$, (b) 0DC, and (c) $+0.5 \cdot I_{20}$.

Table 5. Correlation coefficient between DCA (EN) partial results and EIS parameters.

		$I_{DC} = -0.5 \cdot I_{20}$	$I_{DC} = 0 \text{ DC}$	$I_{DC} = +0.5 \cdot I_{20}$
I_c at 80% SoC	$1/R_1$	0.386	0.105	0.660
	$1/R_2$	0.641	-0.347	0.225
	CPE_1	-0.036	0.524	0.435
	CPE_2	0.105	0.344	0.366
I_d at 80% SoC	$1/R_1$	0.706	0.499	0.876
	$1/R_2$	0.624	0.812	0.622
	CPE_1	-0.230	0.228	0.198
	CPE_2	0.337	0.600	0.521

Comparing the DCA (EN) test results with the EIS measurements, the first semicircle, consisting of the parameters R_1 and CPE_1 , showed a higher correlation than the second semicircle. This was already found in previous publications [21] and falls into place with the observations during single-pulse measurements at different SoC, shown in Section 3.3. Furthermore, the highest correlation was found between the EIS parameters of the first semicircle and the DCA with a superimposed DC current of $+0.5 \cdot I_{20}$. The DCA most likely shows its correlations with the EIS parameters when charging processes are promoted [21]. A good correlation between the capacitance values CPE_1 , which was in the range of double-layer capacitance ($\sim 100 \text{ F}$), and DCA was found.

3.3. Influence of SoC on DCA and EIS

Figure 11 shows the test results of the single-pulse charge acceptance test after charge and after discharge, exemplary for three 3P2N EFB cells. The SoC influence (higher DCA for lower SoC [5–7]) and the differences between additives are visible in the single-pulse DCA test as well. For test cells with DCA-enhancing additives, the effect flattened for a lower SoC, as already shown in previous publications [5–7], while the DCA almost linearly increased for test cells with an overall lower DCA. The influence of prior usage ($I_c < I_d$ [5–10]) was also very clear for the three different test cells Figure 11. It was shown that the influence of prior usage was more distinct than the influence of the SoC. Furthermore, the influence of the SoC and differences between additives are more distinct after discharge than after charge, previously shown in [9,10].

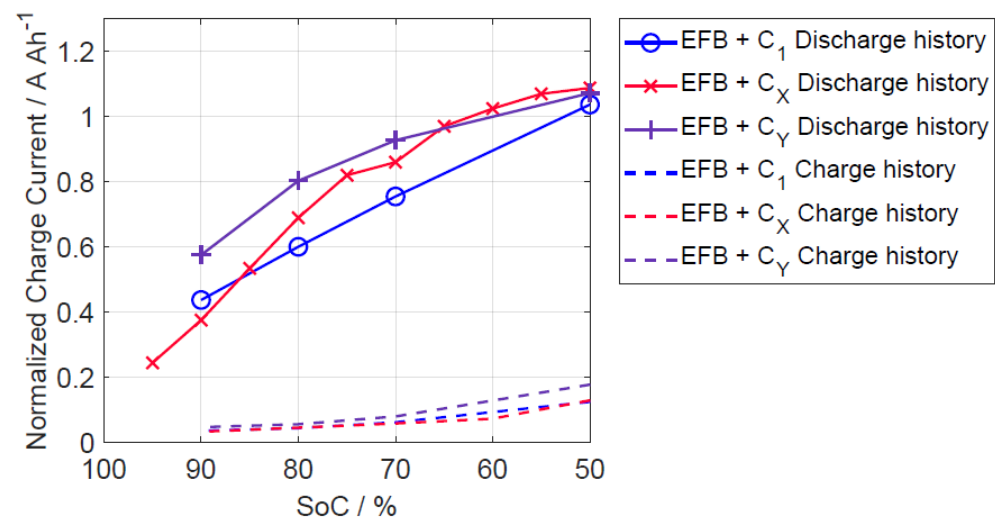


Figure 11. Single-pulse charge acceptance test after prior charge and discharge.

Within Figures 12 and 13, the fitting parameters $1/R_1$, $1/R_2$, CPE_1 , and CPE_2 of the EIS with a superimposed DC current of $+0.5 \cdot I_{20}$ are compared with the single-pulse DCA test results at different SoCs, and their correlation is visualized via the grey dotted line. The correlation coefficients are summarized in Table 6. The correlation between DCA and the parameters obtained during EIS with a superimposed DC current of $+0.5 \cdot I_{20}$ were visualized because they showed the highest correlation compared to the results obtained with superimposed $-0.5 \cdot I_{20}$ or 0DC (Appendix A Figures A7–A10). Moreover, the first semicircle, consisting of the parameters R_1 and CPE_1 , showed a higher correlation than the second semicircle did. Both were observed in earlier publications, as DCA is the most likely to show correlations with EIS parameters when charging processes are promoted and the 10 s DCA pulse has a frequency of 1/10 Hz, which is found in the first semicircle of the EIS spectra [21].

Differences between the single-pulse charge acceptance test at 80% SoC, shown in Figure 11, and the results from EN standard I_c at 80% SoC, shown in Figure 6a, and the I_d at 80% SoC, shown in Figure 6b, are to be expected due to the different test procedures. During the DCA EN test, 20 pulses were evaluated, where the first pulse resulted in the lowest DCA out of all the pulses (0.2–0.3 A Ah⁻¹ incline). Therefore, the DCA EN test results were higher than those of the single-pulse tests.

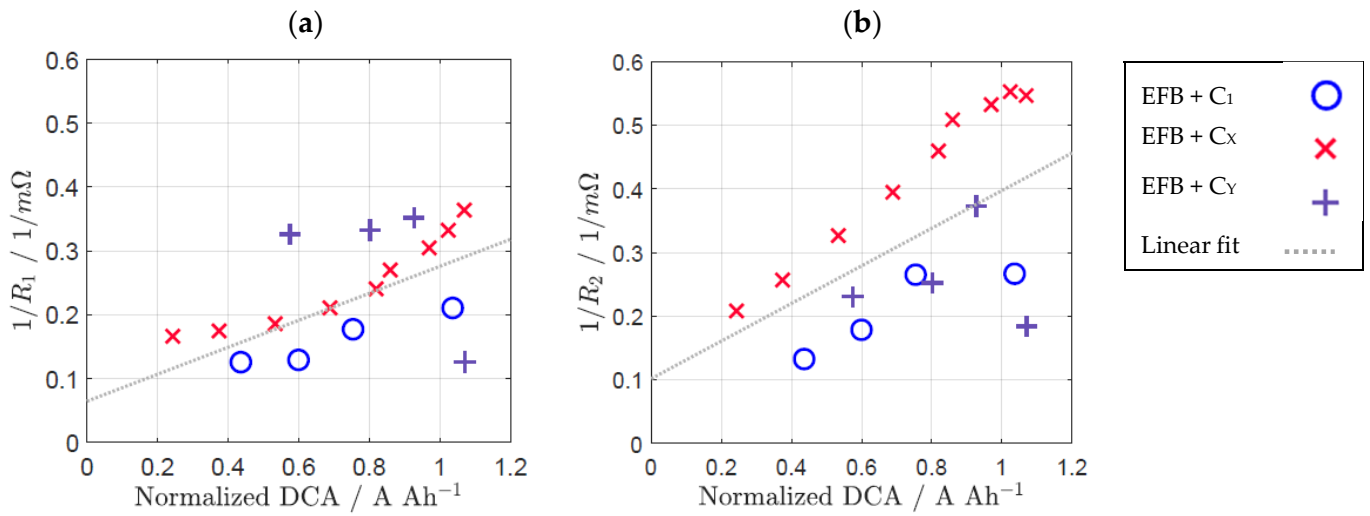


Figure 12. Comparison of single-pulse DCA with fitting parameters (a) $1/R_1$ and (b) $1/R_2$ of EIS with $I_{DC} = +0.5 \cdot I_{20}$ after prior discharge.

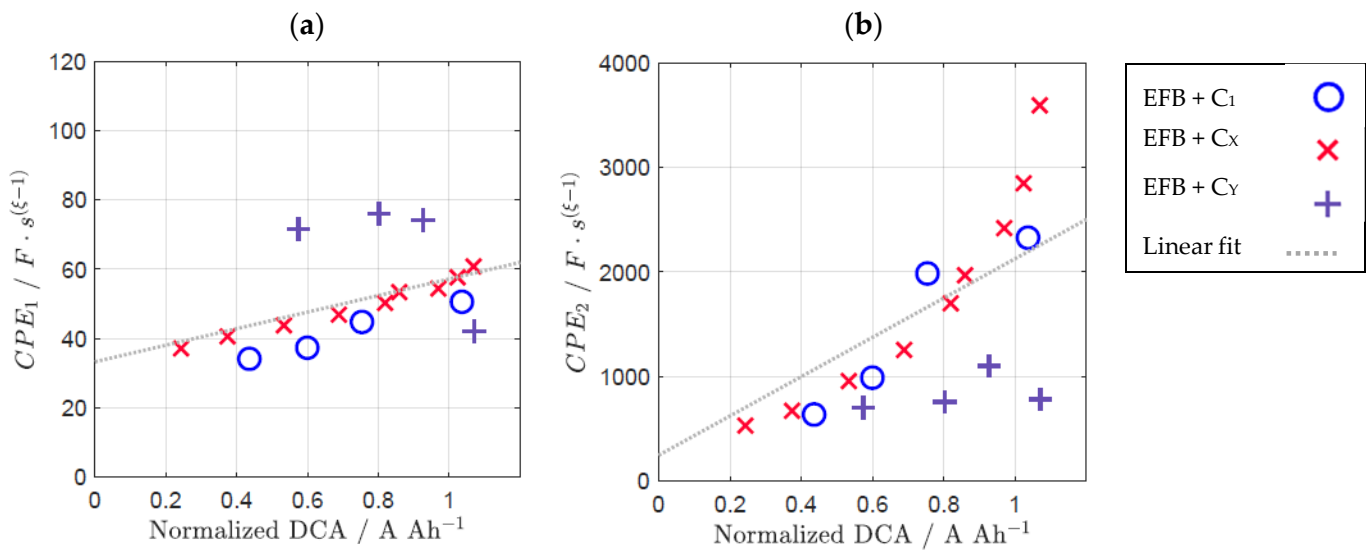


Figure 13. Comparison single-pulse DCA with fitting parameters (a) CPE_1 and (b) CPE_2 of EIS with $I_{DC} = +0.5 \cdot I_{20}$ after prior discharge.

Table 6. Correlation coefficient between the single-pulse DCA after discharge and the EIS parameters after discharge with a superimposed DC current $+0.5 \cdot I_{20}$.

	Complete Correlation Coefficient	Correlation Coefficient of EFB + C_1	Correlation Coefficient of EFB + C_X	Correlation Coefficient of EFB + C_Y
$1/R_1$	0.730	0.996	0.944	0.986
$1/R_2$	0.731	0.878	0.994	0.972
CPE_1	0.636	0.975	0.987	0.417
CPE_2	0.735	0.900	0.939	0.956

4. Conclusions

Eight different NAM formulations were investigated regarding their DCA. Among them, five different amorphous carbons with significant variation of the specific external surface area, two commercially used additive mixes that enhanced DCA, and a commercially available carbon black were used.

DCA was tested with a single-pulse approach and with a modified and shortened version of the EN standard. Thereby, the influence of the additives, the short-term history, and the SoC on DCA could be evaluated. Furthermore, EIS was conducted with identical test cells at various SoC, superimposed DC currents, and charging/discharging histories. The EIS data were preprocessed with a K–K transformation to verify that all evaluated data were stable, causal, and that real and imaginary parts were interdependent [28,29]. Furthermore, the EIS data were investigated via the DRTs to analyze the number of processes and their characteristic frequencies. The EIS measurements were evaluated using an ECM based on DRTs. The high frequency part of the spectra was fitted with internal resistance, inductance, and one CPE but kept constant independent of the investigated SoCs, prior usage, or carbon additives. Only the parameters of the first and second semicircles were freely fitted. Even though this restriction caused a noticeable deterioration of fitting quality, it had to be accepted to validate such a broad range of test cells (additives) and battery states (SoC and prior usage). Artifacts can be avoided only if the model with a minimal number of variable parameters is used. This way, a comparison between the remaining parameters and DCA was possible. Therefore, the gained parameters were correlated with the respective DCA results.

It has been shown that the best parameters for predicting DCA are found within the first semicircle of the negative half-cell spectra measured during a superimposed charging current. By evaluating these parameters, it is possible to quantitatively predict DCA for different additives. Furthermore, the influence of prior usage and the SoC while taking the measurement can also be visualized using EIS.

Author Contributions: Conceptualization, S.B.; methodology, S.B. and J.K.; software, S.B.; validation, S.B. and J.K.; formal analysis, S.B.; investigation, S.B.; resources, S.B.; data curation, S.B.; writing—original draft preparation, S.B.; writing—review and editing, S.B.; J.K., J.S., M.F., and E.K.; visualization, S.B.; supervision, J.K.; project administration, S.B.; funding acquisition, J.K. All authors have read and agreed to the published version of the manuscript.

Funding: This research was funded by the Consortium of Battery Innovation, grant number: 60-1908. We acknowledge the support by the German Research Foundation and the Open Access Publication Fund of TU Berlin.

Institutional Review Board Statement: Not applicable.

Informed Consent Statement: Not applicable.

Data Availability Statement: For any details regarding the reported data, please contact S. Bauknecht via e-mail: sophia.bauknecht@tu-berlin.de.

Acknowledgments: The authors would like to thank Benjamin Hübner, Begüm Bozkaya, Eberhard Meißner, and Matt Raiford for their continuous feedback during countless discussions.

Conflicts of Interest: The authors declare no conflict of interest. The funders had no role in the design of the study; in the collection, analyses, or interpretation of data; in the writing of the manuscript, or in the decision to publish the results.

Abbreviations

AC	alternating current	I_{DCA}	resulting dynamic charge acceptance current
C_{20}	20 h discharge capacity	I_r	average charge current during real-world micro cycles
C_n	nominal capacity	K–K	Kramers–Kronig
CPE	constant phase element	LAB	lead-acid battery
DC	direct current	LSM	laser scanning microscope
DCA	dynamic charge acceptance	N	negative plate
d_{part}	average particle size	NAM	negative active mass
DRT	distribution of relaxation times	P	positive plate
ECM	equivalent circuit model	PAM	positive active mass
EIS	electrochemical impedance spectroscopy	R	resistance
EFB	enhanced flooded batteries	R_0	internal resistance
EFB + C	enhanced flooded batteries with current increasing additives	R^2	correlation coefficient
EN	European standard	RC	resistance-capacity
f_{max}	maximum frequency	Ref-CB	reference, carbon-black
f_{min}	minimum frequency	RH	relative humidity
$I_{AC,max}$	maximum AC current	RSS	sum of squares of residuals
I_{20}	20 h discharge current	SoC	state of charge
I_c	average charge current after prior charge	S_{ext}	specific external surface area
I_d	average charge current after prior discharge	T	temperature
I_{DC}	DC current	TSS	total sum of squares
		τ	time constant

Appendix A

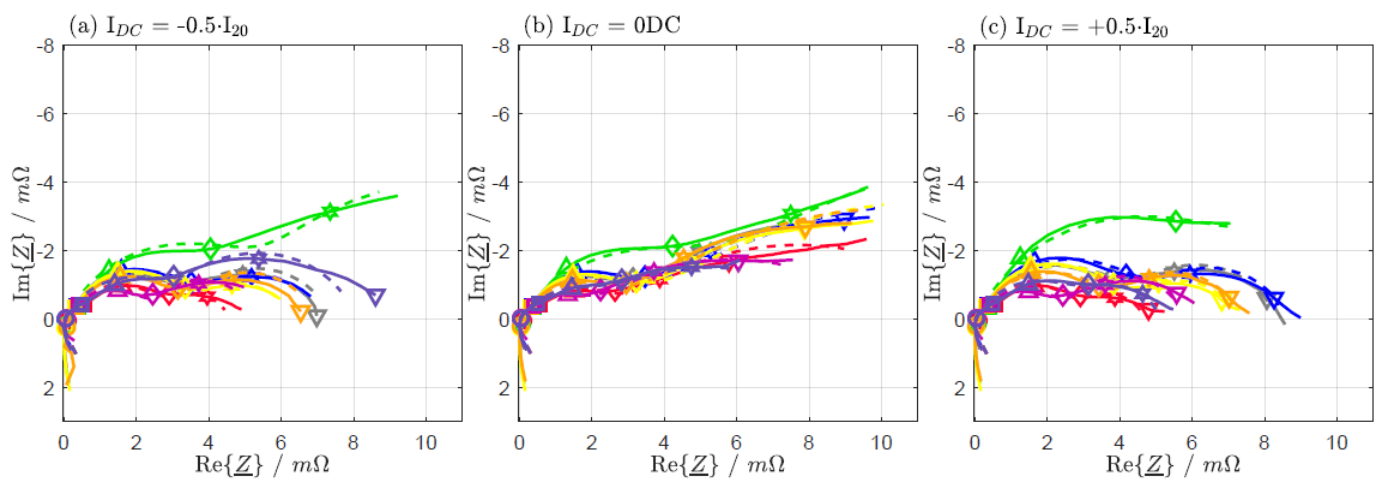
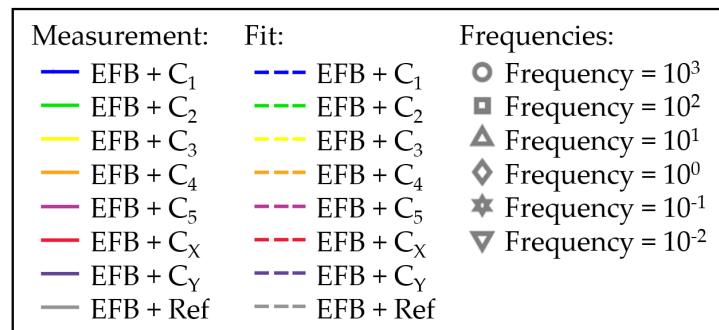


Figure A1. Negative half-cell EIS after prior discharge at 90% SoC with $I_{DC} =$ (a) $-0.5 \cdot I_{20}$, (b) 0DC, and (c) $+0.5 \cdot I_{20}$.

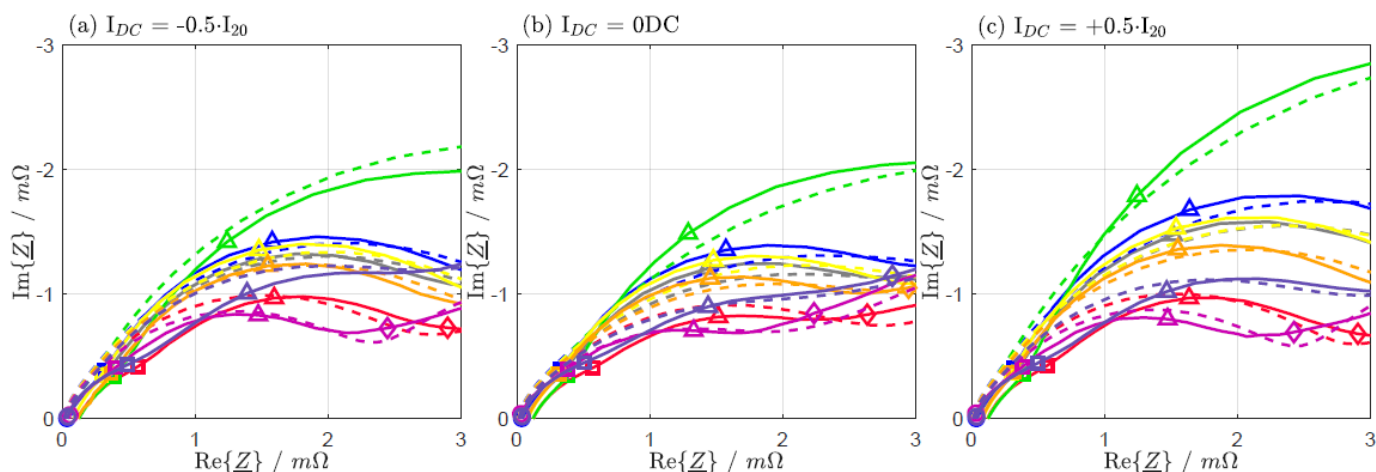


Figure A2. Zoom into negative half-cell EIS after prior discharge at 90% SoC with $I_{DC} =$ (a) $-0.5 \cdot I_{20}$, (b) 0DC, and (c) $+0.5 \cdot I_{20}$.

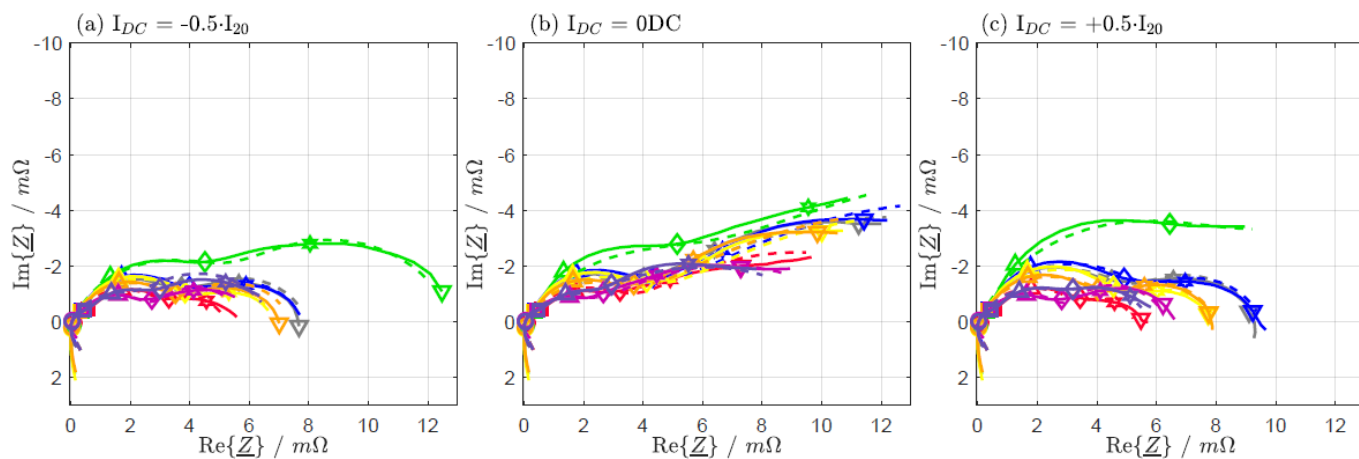


Figure A3. Negative half-cell EIS after prior discharge at 80% SoC with $I_{DC} =$ (a) $-0.5 \cdot I_{20}$, (b) 0DC, and (c) $+0.5 \cdot I_{20}$.

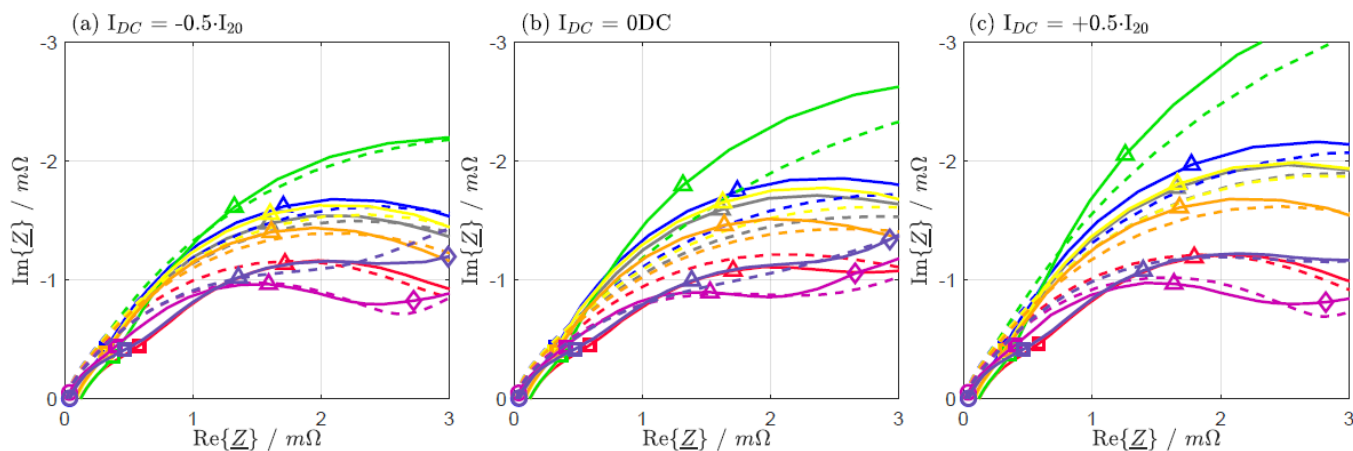


Figure A4. Zoom into negative half-cell EIS after prior discharge at 80% SoC with $I_{DC} =$ (a) $-0.5 \cdot I_{20}$, (b) 0DC, and (c) $+0.5 \cdot I_{20}$.

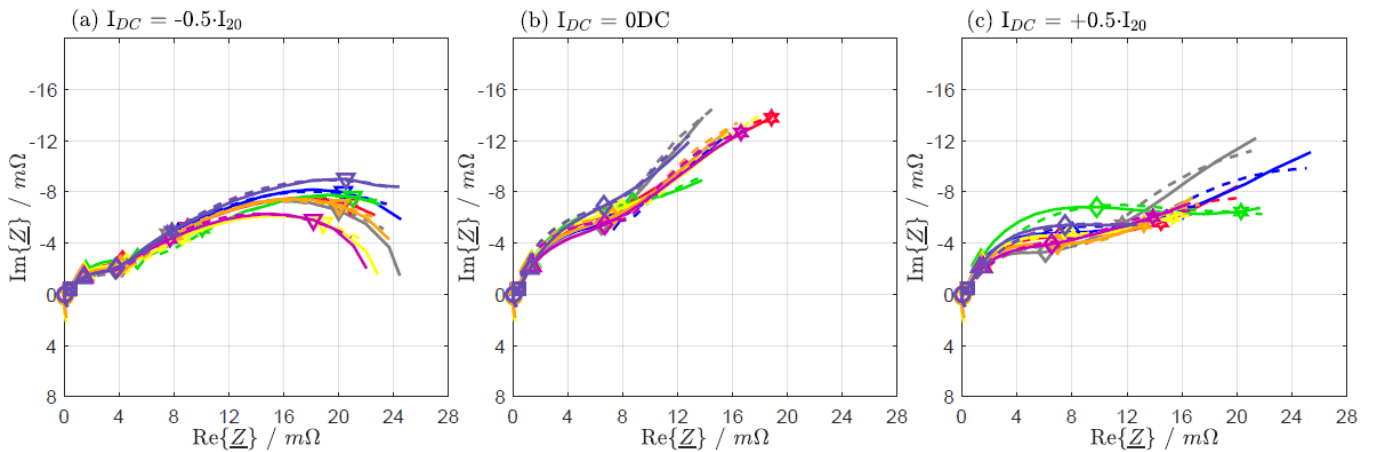


Figure A5. Negative half-cell EIS after prior charge at 80% SoC with $I_{DC} =$ (a) $-0.5 \cdot I_{20}$, (b) 0DC, and (c) $+0.5 \cdot I_{20}$.

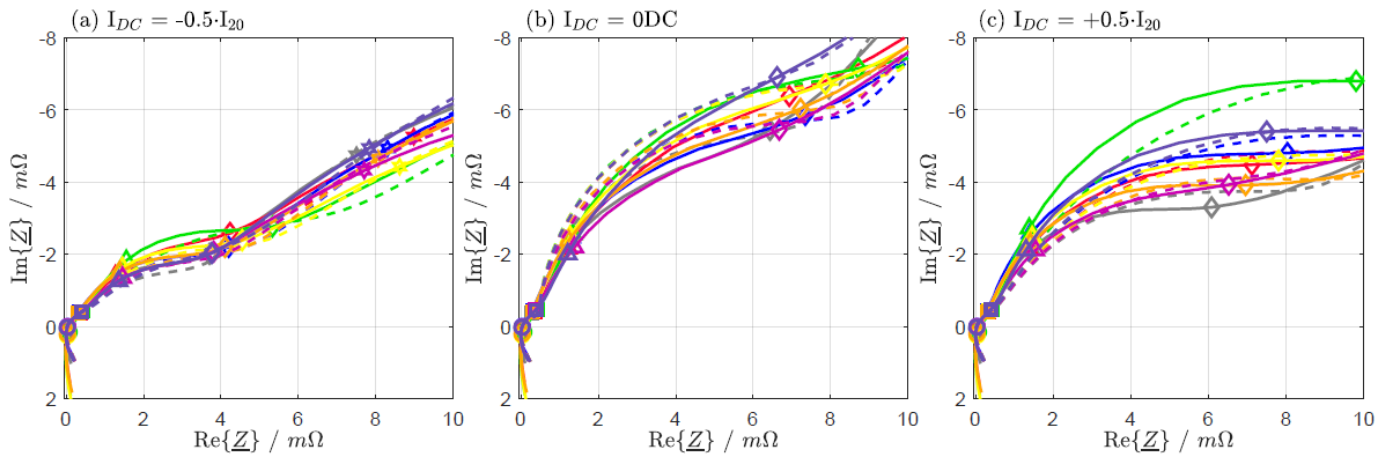


Figure A6. Zoom into negative half-cell EIS after prior charge at 80% SoC with $I_{DC} =$ (a) $-0.5 \cdot I_{20}$, (b) 0DC, and (c) $+0.5 \cdot I_{20}$.

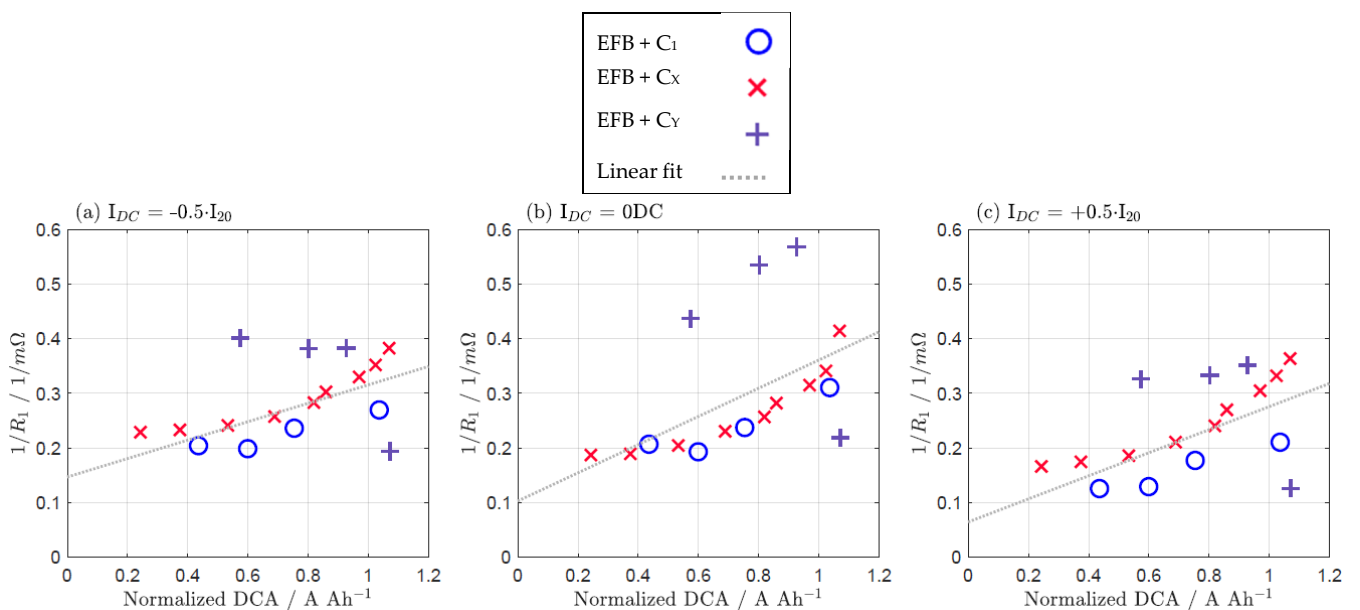


Figure A7. Comparison of single-pulse DCA with fitting parameter $1/R_1$ after prior discharge.

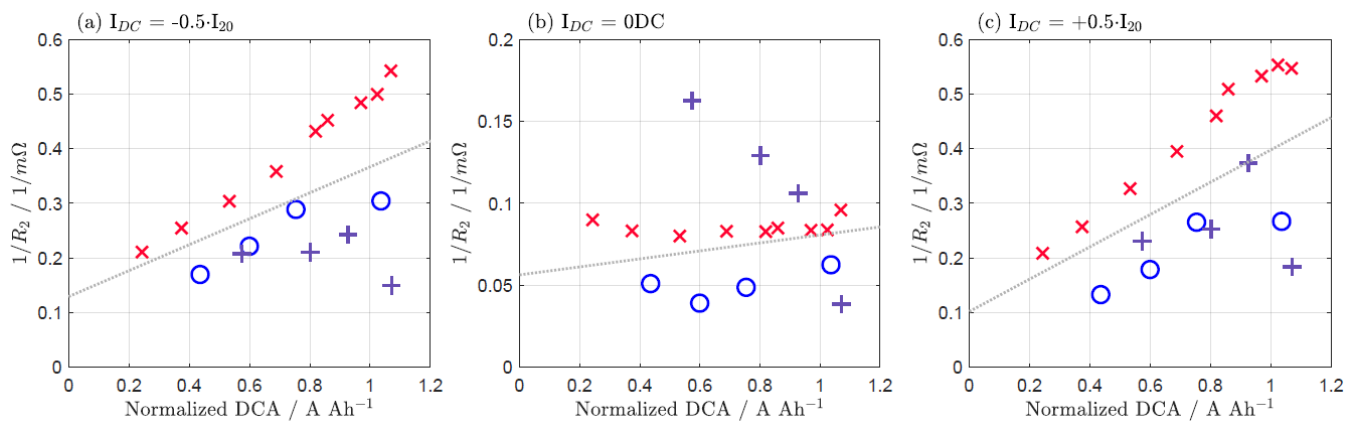


Figure A8. Comparison of single-pulse DCA with fitting parameter $1/R_2$ after prior discharge.

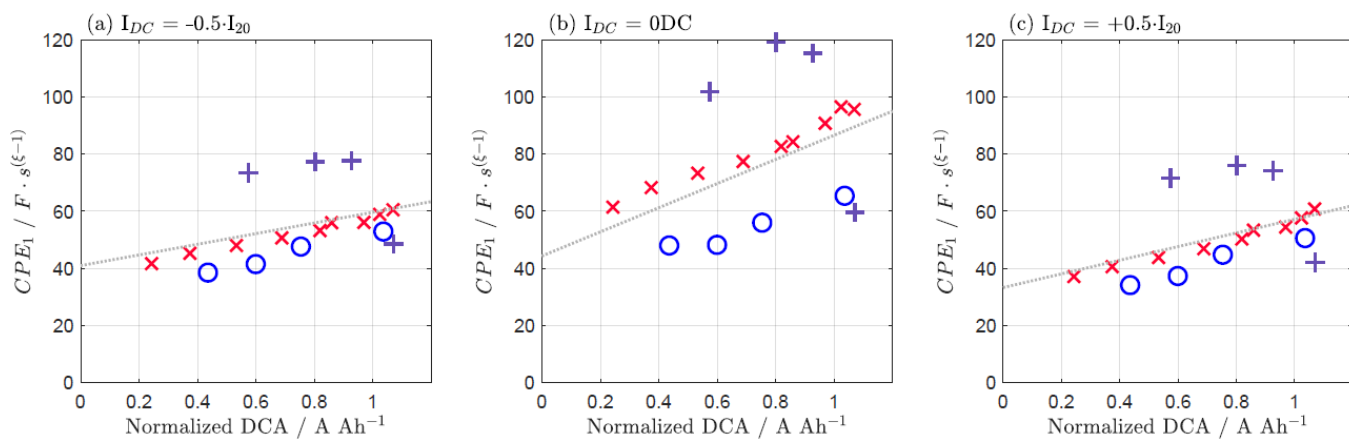


Figure A9. Comparison of single-pulse DCA with fitting parameter CPE_1 after prior discharge.

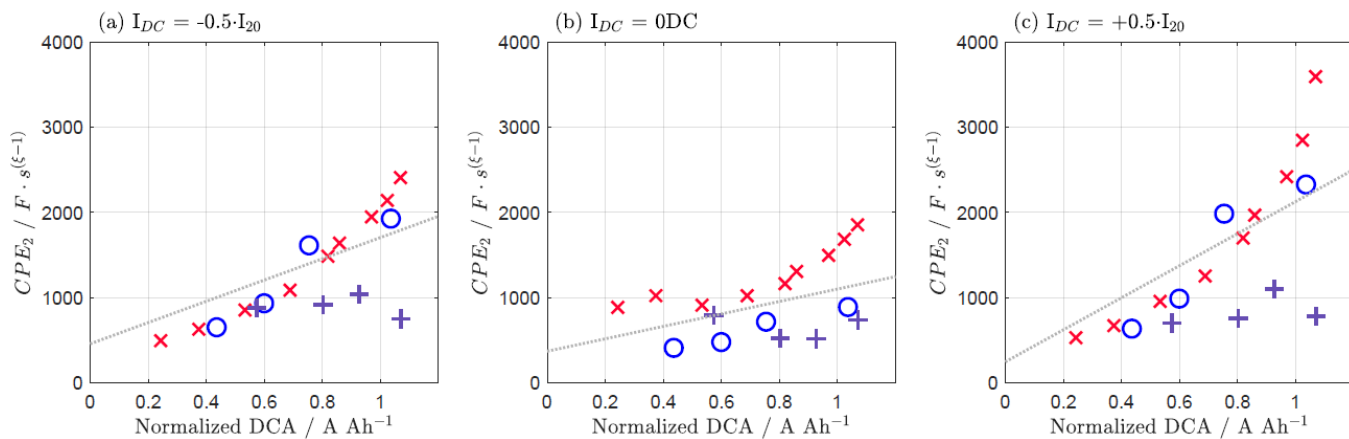


Figure A10. Comparison of single-pulse DCA with fitting parameter CPE_2 after prior discharge.

Table A1. Correlation coefficient between single-pulse DCA after discharge and EIS parameters after discharge for different superimposed DC currents.

	$I_{DC} = -0.5 \cdot I_{20}$	$I_{DC} = 0 \text{ DC}$	$I_{DC} = +0.5 \cdot I_{20}$
$1/R_1$	0.666	0.591	0.735
$1/R_2$	0.449	0.338	0.650
CPE_1	0.545	0.652	0.687
CPE_2	0.480	0.419	0.481

References and Notes

1. SBA S 0101:2014; Battery Association of Japan, Lead-Acid Batteries for Vehicles with Stop and Start System. Battery Association of Japan: Tokyo, Japan, 2014.
2. EN 50342-6:2015; Lead-Acid Starter Batteries—Part 6: Batteries for Micro-Cycle Applications. European Committee for Electrotechnical Standardisation: Brussels, Belgium, 2015.
3. FreedomCAR Battery Test Manual for Power-Assist Hybrid Electric Vehicles; DOE/ID-11069; INEEL: Santa Clara, CA, USA, 2003.
4. Karden, E.; Jöris, F.; Budde-Meiwes, H.; Sauer, D.U. Proceedings of the 13ELBC European Lead Battery Conference, Paris, France, 6–9 September 2012.
5. Budde-Meiwes, H. Dynamic Charge Acceptance of Lead-Acid Batteries for Micro-Hybrid Automotive Applications. Ph.D. Thesis, RWTH Aachen University, Aachen, Germany, 2016.
6. Smith, M.J.; Gladwin, D.T.; Stone, D.A. Experimental analysis of Dynamic Charge Acceptance test conditions for lead-acid and lithium iron phosphate cells. *J. Energy Storage* **2017**, *12*, 55–65. [[CrossRef](#)]
7. Sauer, D.U. DCAX_results_NEDC15_2007-01-24.xls, *Vorlesung Batteriespeichersysteme*, RWTH Aachen, ISEA . 2007.
8. Sauer, D.U.; Karden, E.; Fricke, B.; Blanke, H.; Thele, M.; Bohlen, O.; Schiffer, J.; Gerschler, J.B.; Kaiser, R. Charging performance of automotive batteries—An underestimated factor influencing lifetime and reliable battery operation. *J. Power Sources* **2007**, *168*, 22–30. [[CrossRef](#)]
9. Bozkaya, B.; Bauknecht, S.; Settelein, J.; Kowal, J.; Karden, E.; Giffin, G.A. Comparison of Dynamic Charge Acceptance Tests on Lead-Acid Cells for Carbon Additive Screening. *Energy Technol.* **2022**, *10*, 2101051. [[CrossRef](#)]
10. Bauknecht, S.; Kowal, J.; Bozkaya, B.; Settelein, J.; Karden, E. The Influence of Cell Size on Dynamic Charge Acceptance Tests in Laboratory Lead-Acid Cells. *Energy Technol.* **2022**, *10*, 2101053. [[CrossRef](#)]
11. Pavlov, D.; Petkova, G.; Rogachev, T. Influence of H₂SO₄ concentration on the performance of lead-acid battery negative plates. *J. Power Source* **2008**, *175*, 586–594. [[CrossRef](#)]
12. Thele, M.; Karden, E.; Surewaard, E.; Sauer, D.U. Impedance-based overcharging and gassing model for VRLA/AGM batteries. *J. Power Source* **2006**, *158*, 953–963. [[CrossRef](#)]
13. Budde-Meiwes, H.; Schulte, D.; Kowal, J.; Sauer, D.U.; Hecke, R.; Karden, E. DCA of lead acid batteries comparison of methods for conditioning and testing. *J. Power Source* **2012**, *207*, 30–36. [[CrossRef](#)]
14. Schaeck, S.; Stoermer, A.; Albers, J.; Weirather-Koestner, D.; Kabza, H. Lead-acid batteries in micro-hybrid applications. Part II. Test proposal. *J. Power Source* **2011**, *196*, 1555–1560. [[CrossRef](#)]
15. Moseley, P.T.; Rand, D.A. Partial State-of-Charge Duty: A Challenge but Not a Show-Stopper for Lead-Acid Batteries! *Electrochem. Soc.* **2012**, *41*, 3–16. [[CrossRef](#)]
16. Moseley, P.T. Consequences of including carbon in the negative plates of Valve-regulated Lead-Acid batteries exposed to high-rate partial-state-of-charge operation. *J. Power Sources* **2009**, *191*, 134–138. [[CrossRef](#)]
17. Pavlov, D.; Rogachev, T.; Nikolov, P.; Petkova, G. Mechanism of action of electrochemically active carbons on the processes that take place at the negative plates of lead-acid batteries. *J. Power Sources* **2009**, *191*, 58–75. [[CrossRef](#)]
18. Pavlov, D.; Nikolov, P. Capacitive carbon and electrochemical lead electrode systems at the negative plates of lead-acid batteries and elementary processes on cycling. *J. Power Sources* **2013**, *242*, 380–399. [[CrossRef](#)]
19. Pavlov, D.; Nikolov, P.; Rogachev, T. Influence of expander components on the processes at the negative plates of lead-acid cells on high-rate partial-state-of-charge cycling. Part II. Effects of carbon additives on the processes of charge and discharge of negative plates. *J. Power Sources* **2010**, *195*, 4444–4457. [[CrossRef](#)]
20. Calábek, M.; Micka, K.; Krivák, P.; Baca, P. Significance of carbon additive in negative lead-acid battery electrodes. *J. Power Sources* **2006**, *158*, 864–867. [[CrossRef](#)]
21. Bauknecht, S.; Kowal, K.; Bozkaya, B.; Settelein, J.; Karden, E. Electrochemical Impedance Spectroscopy as an Analytical Tool for the Prediction of the Dynamic Charge Acceptance of Lead-Acid Batteries. *Batteries* **2022**, *8*, 66. [[CrossRef](#)]
22. Bavarian Center for Applied Energy Research (ZAE Bayern). Magdalene-Schoch-Strasse 3, 97074 Würzburg, Germany. Available online: <https://www.zae-bayern.de/> (accessed on 1 February 2023).
23. Scherdel, C.; Scherb, T.; Reichenauer, G. Spherical porous carbon particles derived from suspensions and sediments of resorcinol-formaldehyde particles. *Carbon* **2009**, *47*, 2244–2252. [[CrossRef](#)]
24. Settelein, J.; Oehm, J.; Bozkaya, B.; Leicht, H.; Wiener, M.; Reichenauer, G.; SEXTL, G. The external surface area of carbon additives as key to enhance the dynamic charge acceptance of lead-carbon electrodes. *J. Energy Storage* **2018**, *15*, 196–204. [[CrossRef](#)]
25. Bauknecht, S.; Kowal, J.; Bozkaya, B.; Settelein, J.; Karden, E. The effects of cell configuration and scaling factors on constant current discharge and dynamic charge acceptance in lead-acid batteries. *J. Energy Storage* **2022**, *45*, 103667. [[CrossRef](#)]
26. EN 50342-1 (VDE 0510-101:2019-05); Lead-Acid Starter Batteries—Part 1: General Requirements and Methods of Test. European Committee for Electrotechnical Standardisation: Brussels, Belgium, 2019.
27. Karden, E.; Buller, S.; De Doncker, R.W. A method for measurement and interpretation of impedance spectra for industrial batteries. *J. Power Sources* **2000**, *85*, 72–78. [[CrossRef](#)]
28. Kramers, H.A. Die Dispersion und Absorption von Röntgenstrahlen. *Phys. Z* **1929**, *30*, 522–523.
29. Kronig, R.D.L. On the theory of dispersion of X-rays. *J. Opt. Soc. Am.* **1926**, *12*, 547–557. [[CrossRef](#)]
30. Danzer, M.A. Generalized Distribution of Relaxation Times Analysis for the Characterization of Impedance Spectra. *Batteries* **2019**, *5*, 53. [[CrossRef](#)]

31. Schmidt, J.P.; Chrobak, T.; Ender, M.; Illig, J.; Klotz, D.; Ivers-Tiffée, E. Studies on LiFePO₄ as cathode material using impedance spectroscopy. *J. Power Sources* **2011**, *196*, 5342–5348. [[CrossRef](#)]
32. Meissner, E. NAM Classics: Is low DCA caused by Ostwald Ripening? DCA and Heat Workshop 17–19 November. 2020.

Disclaimer/Publisher's Note: The statements, opinions and data contained in all publications are solely those of the individual author(s) and contributor(s) and not of MDPI and/or the editor(s). MDPI and/or the editor(s) disclaim responsibility for any injury to people or property resulting from any ideas, methods, instructions or products referred to in the content.